ACS APPLIED MATERIALS & INTERFACES

Research Article

www.acsami.org

Semi-Transparent ZnO-CuI/CuSCN Photodiode Detector with Narrow-Band UV Photoresponse

Zhi Yang,[†] Minqiang Wang,[*,†] Jijun Ding,[†] Zhongwang Sun,[†] Le Li,[†] Jin Huang,[†] Jing Liu,[†] and Jinyou Shao[‡]

[†]Electronic Materials Research Laboratory (EMRL), Key Laboratory of Education Ministry; International Center for Dielectric Research (ICDR), Xi'an Jiaotong University, Xi'an 710049, China

[‡]State Key Laboratory of Manufacturing Systems Engineering, Xi'an Jiaotong University, Xi'an 710049, China

Supporting Information

ABSTRACT: The ZnO homogeneous pn junction photodiode is quite difficult to fabricate due to the absence of stable p-type ZnO. So exploring reliable p-type materials is necessary to build a heterogeneous pn junction with n-type ZnO. Herein, we develop a simple and low-cost solution-processed method to obtain inorganic p-type CuI/CuSCN composite film with compact morphology, high conductivity, and low surface state. The improved performance of CuI/CuSCN composite film can be confirmed based on high-rectification ratio, responsivity, and open voltage of ZnO-CuI/CuSCN photodiode UV detectors. Moreover, photodiodes with novel top electrodes are investigated. Compared with commonly used Au and graphene/Ag nanowire (NWs) electrode, poly(3,4-ethylenedioxythiophene):poly(4-styrenesulfonate) (PEDOT:PSS) electrode prepared by Meyer rod-coating technique opens one route to obtain a semitransparent photodiode. The photodiode with PEDOT:PSS as the top electrode under reverse illumination has the highest photocurrent density due to higher UV transmittance of PEDOT:PSS transparent electrode compared with ITO glass. The low-energy consumption, and high responsivity, UV to visible rejection ratio and air stability make this ZnO-CuI/CuSCN photodiode quite promising in the UV-A detection field.

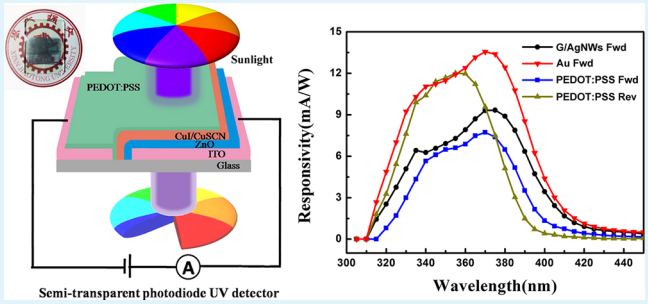

KEYWORDS: *inorganic p-type films, photodiode, PEDOT:PSS electrode, semitransparent, ZnO UV detectors*

1. INTRODUCTION

For decades, UV photodetectors have played the crucial role in a wide range of applications in fire monitoring, optical communications, and UV irradiation detections.[1,2] Nanostructured photodetectors have two main structures: a photoconductor and a photodiode. The photoconductor type only conducts a single carrier type, making it unipolar, which usually has high gain and long response and recovery times. In contrast, the photodiode type can extract both electron and hole through built-in potential, resulting in high responsivity and fast response speed.[3] What's more, the nanostructured photodiode detector can work at a self-powered mode, meaning a huge current increase at 0 V employing photovoltaic property. So the photodiode UV detector also meets the requirement of low-energy consumption and small size.[4]

ZnO, an environmentally friendly material, has been widely used in UV detection field due to its large band gap (3.35 eV), excellent electron transporting property, and a variety of morphologies obtained by solution-processed and magnetron sputtering methods. Previously, ZnO-based UV photodetectors have been widely reported based on both photoconductor and photodiode structures. For example, we have prepared ZnO/Ag NWs/ZnO composite films photoconductor UV detector.[5] But the response and recovery times were still not short enough. The ZnO nanorod metal−semiconductor−metal photodetector Su et al. fabricated also had long recovery time of 15.44 s due to prominent persistent photoconductivity (PPC) effect.[6] Thus, the slow response and recovery speeds are the main problem that existed in the photoconductor detector. However, the ZnO NWs/CuSCN photodiode Hatch et al. prepared[7] and ZnO NWs/Spiro-MeOTAD Game et al. prepared[8] had only 6.7 μs and 0.95 ms recovery time, respectively, indicating very fast operation speed of the photodiode detector. Later in the paper, their photoresponse parameters and test conditions are compared with our photodiodes made here.

P-type ZnO is necessary to build a homogeneous pn junction photodiode. However, it still remains a challenge to obtain stable p-type ZnO by incorporating acceptor defects effectively.[9] So a variety of p-type materials are used to build heterogeneous pn junction with n-type ZnO, including Spiro-MeOTAD,[8] P3HT,[10] PEDOT:PSS,[11] NiO,[12] CuO,[13] Si,[14] etc. Recently, copper iodide (CuI) and copper thiocyanate

Received: June 14, 2015
Accepted: September 9, 2015
Published: September 9, 2015

DOI: 10.1021/acsami.5b05222
ACS Appl. Mater. Interfaces 2015, 7, 21235−21244

(CuSCN) as cheap and solution-processed inorganic p-type materials have attracted people's interest because they could be used as hole transporting layer to obtain remarkable efficiency in perovskite solar cells[15−18] compared with their organic counterparts. Besides, they are quite stable in air and not affected by moisture, which is the main reason to make organic p-type material degradation. γ-Phase CuI film with a band gap of 3.1 eV has high hole concentration and mobility of 2 cm^2 V^{-1} s^{-1} at least,[19] resulting in higher conductivity than Spiro-MeOTAD and P3HT. However, it usually has a surface trap coming from excess iodine. Christians et al. reported that perovskite solar cells employing CuI as a hole transporting layer had low open-voltage (V_{oc}) due to this surface recombination.[15] In contrast, β-CuSCN film with a wider band gap of 3.9 eV has low hole mobility of 0.01 cm^2 V^{-1} s^{-1}.[20,21] The dye-sensitized[22,23] and perovskite[16] solar cells employing CuSCN have stable V_{oc}, indicating no severe surface trap problem. So an ideal inorganic p-type film is expected combining high conductivity of CuI and low surface trap of CuSCN. Moreover, the intrinsic polymeric structures of CuI and CuSCN enable them to dissolve into suitable solvents, thus rendering them solution-processed property. The spherical aggregates often appear for solution-processed CuI due to the rapid crystals growth and subsequent random agglomeration.[24] These aggregates can develop to be crack or rough surface, which is quite harmful in planar heterojunction device application. The previous research indicated that SCN^- had strong adsorption onto the CuI surface via binding of sulfur to copper sites, which could act as CuI crystal growth inhibitor.[25] So there is reason to believe that smooth and compact composite films can be obtained by mixing CuI and CuSCN, and composite films may have high conductivity and low surface trap density.

Finally, a top electrode (TE) is required to achieve the whole photodiode. Typical laboratory TE is various metal films such as Au, Ag, and Al by thermal evaporation. The Ag and Al TEs with hundreds of nanometers thickness can not exist stably in air for several months, and Au TE can not meet the low-cost requirement, limiting their potential in commercial manufacture. Recently, graphene/Ag NWs (G/AgNWs) composites have been widely used as transparent conductive electrode (TCE),[26−28] flexible electrode,[29] and conductive paper.[30] PEDOT:PSS and its composite are also widely used as TCE in many devices.[31] However, most of these TCEs are used as bottom electrodes replacing ITO. Snaith's group proposed semitransparent solar cells with PEDOT:PSS TE applied to smart windows combining light transmission and energy generation.[32,33] Our semitransparent UV detectors can increase visible light transmission but will not decrease UV light capturing, thus improving UV to visible rejection ratio greatly. More important is that our semitransparent UV detectors do not have the compromise between visible light capturing and transmission for solar cells due to the different region between UV light capturing and visible light transmission. So this ZnO-CuI/CuSCN photodiode UV detector with PEDOT:PSS TE has narrow-band UV photoresponse, reducing false alarm probability. In this paper, ZnO film with suitable thickness and low surface defect density was employed as UV light absorption layer and excellent visible transmittance was obtained. Next, the composite films with different proportion of CuI and CuSCN were investigated from morphology and band to surface state. Then the G/AgNWs conductive paper was employed as TE to fabricate ZnO-CuI/CuSCN photodiode due to its high conductive and flexible properties. Au TE was used as reference, and PEDOT:PSS TE opened one door to obtain semitransparent photodiode. Ag TE was not used to contact CuI and three kinds of composite films directly because it was active enough to form silver halide with CuI,[34] resulting in gradually disappearing photoresponse, and we could find Ag TE color change from the original silvery white to a final yellow brown in just a few days. However, novel G/AgNWs TE could be used to contact halide films, and the photodiode showed good photoresponse stability for two months, indicating graphene plays a role in avoiding direct contact between halide film and Ag NWs. Finally, the photoresponse performances of photodiode with three TEs were compared.

2. EXPERIMENTAL DETAILS

Fabrication of ZnO Layer. The patterned ITO glasses were obtained by wet etching process. In detail, several 3 M tape strips with fixed size were pasted on original ITO glass (produced by Foshan Raching Glass Technology Co., Ltd. The glass thickness is 1.1 mm and sheet resistance is 20 Ω/□) firmly as mask, and then Zn powder and ethanol mixture mash was smeared on above substrate. Next, dilute HCl was dropped, and severe chemical reaction happened to remove ITO. Then the patterned ITO glasses were cleaned by deionized water and acetone and exposed to argon plasma for 2 min to remove organic contaminants. Next, ZnO layer was prepared by magnetron sputtering procedure at 60 °C with ZnO target at a constant ac power of 150 W, and Ar flow of 20 cc. The different thickness of 45, 120, and 250 nm were obtained under 15, 30, and 60 min, respectively. Finally, the ZnO films were treated at 350 °C in air for 60 min. The sputtering method was adopted based on lower surface defect density compared with sol−gel method according to the Ghosh et al. report.[35]

Fabrication of ZnO-CuI/CuSCN Heterojunction Photodiodes. CuI and CuSCN powders were dissolved into di-*n*-propyl sulfide by stirring for 24 h to form 95 and 19 mg/mL solution, respectively. For CuSCN solution, 19 mg/mL is the saturation concentration at room temperature. The concentration of CuI was chosen as 5 times that of CuSCN because we mainly wanted to use high conductivity of CuI and the addition of CuSCN could be confirmed to overcome the surface problem of CuI partly based on the next discussion. In order to study the impact of the surface and band properties of p-type material on device performance, three different mass ratios of 20:1, 10:1, and 5:1 for CuI and CuSCN solution were obtained by mixing original concentration solution. Next, five different p-type films were prepared on ZnO film by spin-coating corresponding solution at 3000 rpm for 60 s. Then they were pretreated at 60 °C for 5 min to evaporate solvent slowly and transferred to 120 °C for 30 min to ensure good crystallization. The whole procedure was carried out in air. Three kinds of TEs including Au, G/AgNWs, and PEDOT:PSS were employed to investigate the charge transfer ability. Au electrode was fabricated on p-type film by thermal evaporation. G/AgNWs composite conductive paper was collected with a polytetrafluoroethylene (PTFE) membrane filter (pore size of 0.2 μm) by vacuum filtration. The mechanical exfoliation graphene in *N*-methyl pyrrolidone with 0.5 mg/mL and AgNWs in ethanol with 10 mg/mL were dropped on PTFE membrane separately one-by-one to obtain multilayer G/AgNWs composite paper. After drying at 100 °C, the G/AgNWs composite electrode with suitable size was fixed on p-type film using 3 M tape adhesive. This G/AgNWs TE has a sheet resistance of 2 Ω/□, which is similar to other's report,[36] and the SEM images in Figure S1 show the uniform mixing characteristics. PEDOT:PSS electrode was fabricated on p-type film by Meyer rod coating technique. Briefly, a Meyer rod pulled over the mixed PEDOT:PSS (Clevios FE T) and methanol solution (1:1 volume), leaving a uniform and thin layer of PEDOT:PSS. This PEDOT:PSS TE has a sheet resistance of 200 Ω/□.

Characterization. Surface morphologies and energy dispersive spectrometer (EDS) were measured by FEI Quatan 250 FEG scanning electron microscope (SEM) and Vecco Innova atomic force microscope (AFM). X-ray diffraction (XRD) measurement was carried

DOI: 10.1021/acsami.5b05222
ACS Appl. Mater. Interfaces 2015, 7, 21235−21244

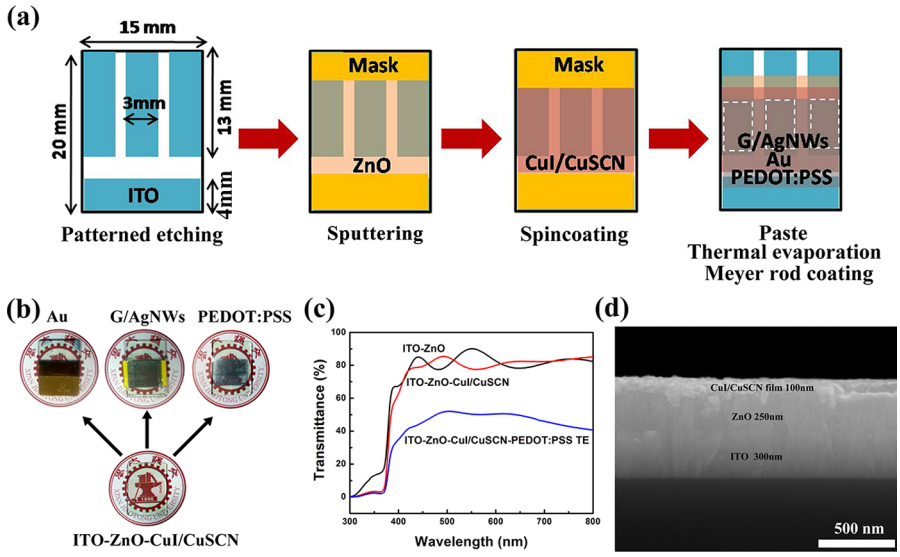

Figure 1. (a) Procedure schematic of preparing photodiode UV detectors, three TEs are employed to compare the performance. A slice of ITO is reserved to connect with TEs. This design can protect novel TEs from damage of electrical clamps. (b) Photographs of devices without and with TEs, (c) the optical transmittance spectra, and (d) cross-section SEM of typical device.

out with a Rigaku D/max 2400 using Cu Kα radiation. Optical absorption and transmittance data were acquired with a Jasco V-570 UV/Visible/NIR spectrophotometer, which had a wavelength range from 190 to 2500 nm. Photoluminescence (PL) spectra were taken with Gilden Photonic Sens-9000 with xenon lamp as the excitation source, and the measurement was conducted in air at room temperature. We chose 350 nm as the excitation wavelength, and integration time was 500 ms. The change of PL spectra could be observed for five kinds of p-type films. X-ray photoelectron spectroscopy (XPS) was measured by Kratos Axis Ultra DLD, using mono Al Kα operated at 150 W. The spectroscopic data were processed using CasaXPS software to obtain the surface chemical composition of different films. IV and time-dependent photoresponse measurements were recorded by Keithley 2400 source meter, and delay time between two test points was 0.1 s. The samples were illuminated under 150 W xenon lamp. The measured spectral irradiance and standard AM 1.5 spectra are shown in Figure S2, and UV irradiances used in the experiment can be estimated as 5.5 mW/cm^2. For time-dependent photoresponse measurement, dark and light states were switched by opening and shielding light source manually. The incident photon-to-current conversion efficiency (IPCE) was measured by the solar cell quantum efficiency measurement system (7-SCSpec II system, NewPort), and step was 5 nm. The wavelength-dependent responsivity spectra was obtained from the expression R = IPCE × λ/1240. Electrochemical impedance spectroscopy (EIS) was recorded using an electrochemical workstation (CHI660D, Chenhua, Shanghai). The measured frequency ranged from 1 Hz to 100 kHz, and the amplitude was set at 1 mV. The spectra were fitted by Zview software.

3. RESULTS AND DISCUSSION

3.1. Structure, Chemical, and Surface Properties of ZnO-CuI/CuSCN Photodiode. Figure 1a describes the procedure of preparing photodiode UV detectors. Compared with commonly used patterned TE structure, we use patterned ITO with fixed size as the bottom electrode, which is quite convenient to study the impact of different TEs on device performance, and the photosensitive areas for all devices are 0.1 cm^2. Compared with opaque Au and G/AgNWs TEs, PEDOT:PSS TE has higher transmittance, making the whole device semitransparent. The photographs of devices in Figure 1b show transparency of the light-absorbing layer, semi-transparency of device with PEDOT:PSS TE, and opaque with Au and G/AgNWs TEs. From the transmittance spectra shown in Figure 1c, we can see transmittance around 80% in the visible region (450−800 nm) for ZnO and ZnO-CuI/CuSCN layers, and the oscillation property comes from optical interference of the very flat film. The decreased transmittance around 400 nm for ZnO-CuI/CuSCN layer derives from the absorption of CuI. For device with PEDOT:PSS TE, the transmittance decreases to 50% in the visible region, indicating semitransparency of the photodiode UV detector. The thickness of each layer can be obtained from cross-section SEM images in Figure 1d and Figure S3. The ZnO thickness of 250 nm can ensure a large amount of UV absorption and not thick enough to decrease the visible transmittance due to optical scattering. However, the thickness of p-type films can be different due to different solution concentration. The thickest CuI film has a thickness of 150 nm, the thinnest CuSCN film has a thickness of 55 nm, and all composite films have thicknesses around 100 nm. Here, we estimate the thickness of depletion layer between ZnO and the p-type film based on reported carrier concentration. The undoped ZnO film by magnetron sputtering method has a very high resistivity of 10^8 Ω cm, and electron concentration is smaller than 10^{12} cm^{-3}.[37,38] However, the solution-processed p-type CuI film has a low resistivity of 1 Ω cm, and hole concentration is 10^{18} cm^{-3}.[39] The solution-processed CuSCN film has a relatively high resistivity of 333 Ω cm, and hole concentration is 7×10^{15} cm^{-3}.[22] For CuI/CuSCN composite films, hole concentration should be closer to CuI film due to its high proportion. So depletion layer almost all falls into the n-type ZnO side based on ideal pn junction model, and the p-type side has little contribution to the photogenerated carriers. So the performance difference of photodiode with five kinds of p-type films can be mainly attributed to photogenerated carriers transport process in pn junction interface and p-type film, which has little relationship with the generation process of photogenerated carrier. This conclusion is quite important to analyze performance difference of five photodiodes, and this speculation can be partially supported by final EIS analysis. Besides, the morphology of sputtered ZnO layer is shown in Figure S4.

DOI: 10.1021/acsami.5b05222
ACS Appl. Mater. Interfaces 2015, 7, 21235−21244

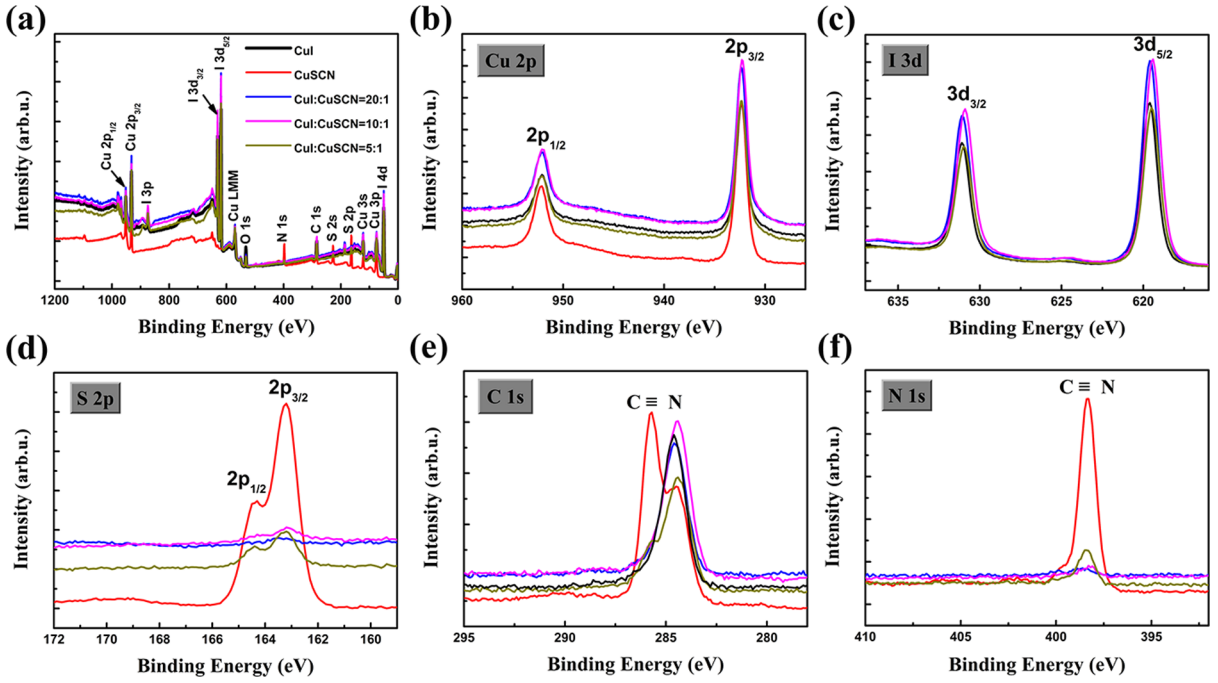

Figure 2. XPS spectra of five p-type films on glass: (a) survey spectra and binding energy spectra of (b) Cu 2p, (c) I 3d, (d) S 2p, (e) C 1s, and (f) N 1s. All peaks are calibrated using C 1s (284.6 eV).

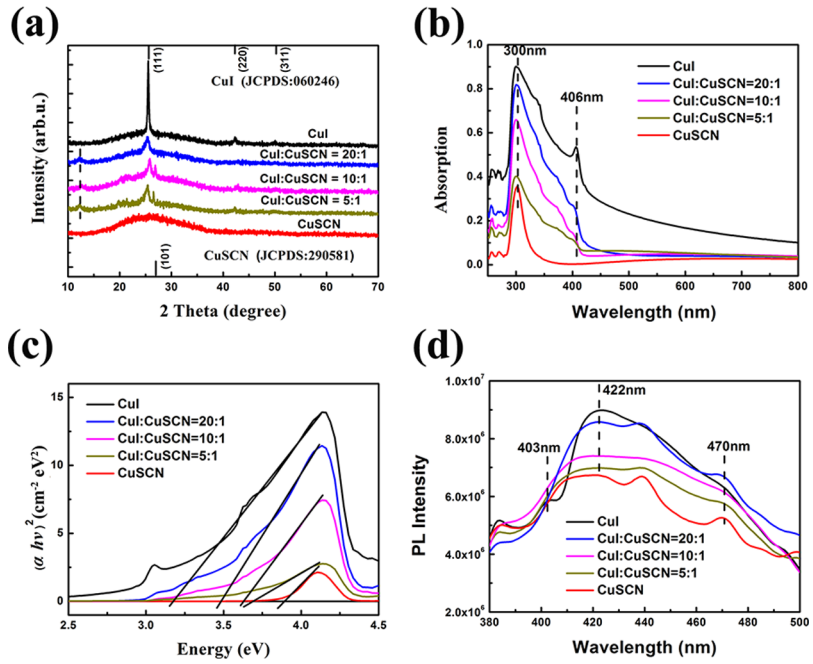

Figure 3. (a) XRD patterns of five p-type films on glass treated at 120 °C, and the standard patterns of bulk cubic CuI and rhombohedral CuSCN are presented as references. CuI film mainly has (111) crystal plane, and CuSCN film mainly has (101) crystal plane. (b) Optical absorbance spectra of five p-type films on glass, the glass absorption is deducted. The featured peak at 406 nm is from CuI, and the peak at 300 nm appears for all films, which may be caused by substrate deduction. The peak from CuSCN can not be identified obviously due to increased short-wavelength absorption for composite films. The absorption intensity difference for five films is attributed to different thickness and different absorption efficiency between CuI and CuSCN. (c) Tauc plot obtained from optical absorbance spectra in (b). (d) PL spectra.

The uniform, smooth, and compact ZnO film in a large area is very beneficial to build planar pn junction photodiode devices.

In order to study the effect of CuI and CuSCN mixed proportion on the film morphology, band, and surface state of p-type hole transporting layer, three different composite films were prepared on Si or glass substrates from different mass ratios of 20:1, 10:1, and 5:1 for CuI and CuSCN mixed solution. The CuI and CuSCN films were also prepared as comparison. For SEM and AFM measurements, five p-type films were obtained by spin-coating solution on Si substrate at 3000 rpm. For XPS, XRD, absorption, and PL measurements, they were obtained by spin-coating solution on glass substrate at 1000 rpm. This solution deposition process can be described as follows. Nucleation occurs with solvent evaporation at the

DOI: 10.1021/acsami.5b05222
ACS Appl. Mater. Interfaces 2015, 7, 21235−21244

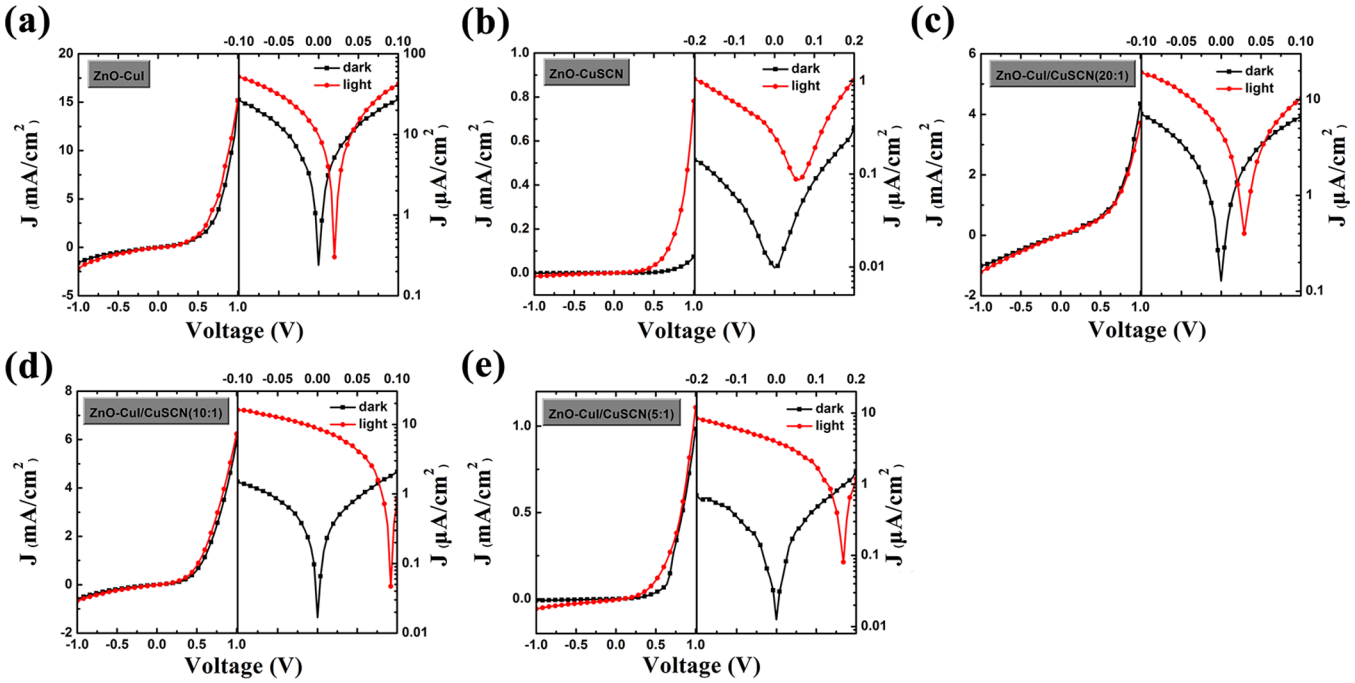

Figure 4. Left parts are *J*−*V* curves obtained under dark and light conditions for (a) ZnO-CuI, (b) ZnO-CuSCN, (c) ZnO-CuI/CuSCN (20:1), (d) ZnO-CuI/CuSCN (10:1), and (e) ZnO-CuI/CuSCN (5:1), and the right parts are corresponding magnified *J*−*V* curves in semilogarithmic scale near 0 V. G/AgNWs TE is used for all five kinds of photodiodes.

initial deposition stage. Then is the rapid self-aggregation growth process of inorganic crystal. Their orientation is favored on smooth surfaces, and they tend to grow along existing crystals to develop a minimum free-energy configuration.[40] So crystal size, continuity, and roughness of film are determined by evaporation rate, substrate surface, and intrinsic growth tendency of the material itself. Before films were made, substrates were treated with argon plasma to produce the hydrophilic and clean surface. The final surface morphologies are shown in Figure S5. From SEM images, CuI film has many obvious cracks, and relatively large average roughness of 6 nm can be seen from the AFM image. In comparison, CuSCN film has the smallest roughness of 1.4 nm. So CuI film has larger crystalline size than CuSCN film, resulting in larger roughness. The crack of CuI film maybe comes from too fast crystal growth rate or large inner stress. For composite films, the roughness decreases with increasing ratio of CuSCN, resulting from the inhibiting growth speed of CuI from SCN^- mentioned above or stress relaxation during this solution-processed procedure. In particular, there exist two kinds of different morphology domains from the SEM image of CuI/CuSCN (20:1) in Figure S5e. The EDS of two different selected areas are used to analyze the element distribution, as shown in Figure S6. The rough domain with the atom ratio of 1:1 between Cu and I elements is pure CuI, while the smooth domain with the atom ratio of 2:1 must be the composite film. This may be caused by inadequate amount of SCN^- inhibiting growth, because we have not found existing the two phase for another two composite films including more CuSCN proportion. Next, the XPS measurement was conducted to analyze the elemental composition of p-type films. The general scan spectra in Figure 2a shows the presence of Cu 2p, I 3d, S 2p, C 1s, and N 1s. For single CuI, Cu $2p_{3/2}$ and I $3d_{5/2}$ have the binding energies of 932.3 and 619.5 eV, respectively, which quite match the pure CuI material in literature.[41] No other byproduct like CuO is found from Cu 2p spectra. The emerging C 1s arises from the adventitious carbon. For single CuSCN, the major peaks in C 1s at 286 eV and N 1s at 398.3 eV are assigned to C≡N bond.[21] The other peak in C 1s at 284.6 eV also comes from the adventitious carbon. Compared with the previous report,[21] there are no peaks of C═N bond, indicating no oxidation happens. For composite films, all peaks of the S−C≡N bond are weak, resulting from a very small amount of CuSCN in composite films, and their intensities are proportional to the amount of CuSCN. The element ratios of five p-type films are summarized in Table S1. We can know the element ratios are very close to the stoichiometric ratios, other than high C content from adventitious carbon. The real proportions of CuI and CuSCN in composite films are also obtained, which are about half of the preset mass ratios. Moreover, the crystallinity of composite films annealed at both 120 and 80 °C are confirmed by XRD in Figure 3a and Figure S7. The diffraction peaks of the CuSCN film can not been seen due to the thinnest thickness. Composite films have both CuI (111) and CuSCN (101) diffraction peaks only at 120 °C, and the intensity is proportional to their amount. The lack of CuSCN diffraction peak at 80 °C may be attributed to increased crystallinity temperature due to the competitive crystal growth between CuI and CuSCN for composite film. The peak at 12° appeared under both 120 and 80 °C treatment belongs to neither CuI or CuSCN, but the reason is not clear. In all, composite films with different ratios of CuI and CuSCN have been confirmed by morphology, element composition analysis, and crystallinity.

Next, we will discuss the impact of different composition on band gap and surface state of composite films. From Figure 3b, the CuI absorbance peaks intensity at 406 nm increase with the increased amount of CuI, while CuSCN absorbance peaks intensity are not quite obvious due to the small amount. All films with low absorbance in the visible region (longer than 450

DOI: 10.1021/acsami.5b05222
ACS Appl. Mater. Interfaces 2015, 7, 21235−21244

nm) are quite helpful to obtain high UV to the visible rejection ratio. Furthermore, the band gap values of CuI and CuSCN films can be obtained from the Tauc plot in Figure 3c. The results in Figure S8 show that the band gaps are almost not changed with the thickness for both CuI and CuSCN films, indicating that band gaps change for composite films are not caused by film thickness. However, band gap concept may be inaccurate to describe the absorbance change for composite films. The difference of Tauc plot for composite film must come from the different proportion between CuI and CuSCN. The reason may be the redistribution of electrons due to the electronegativity difference between I^- and SCN^-, indicating the strong interaction of two anions in composite films. This phenomenon is similar to the Tauc plot change for ZnO/CdS NWs with different CdS content in quantum dot-sensitized solar cells.[42] However, it may be different with band gap variation caused by altering component stoichiometric ratios.[43,44] The proportions of composite films also have an effect on PL spectra. From Figure 3d, CuI film has two PL peaks at 403 and 422 nm, which are ascribed to band-edge emission (~3.1 eV) and surface trap recombination emission (~2.9 eV), respectively.[40] This surface trap comes from excess iodine diffused to the surface from the bulk, acting as an acceptor of electrons to induce p-type conductivity.[45] Zheng et al. thought this surface trap mainly existed in CuI films with the (111) crystal plane.[41] This crystal orientation is in accordance with our XRD results. Besides, the iodine slightly higher than stoichiometric ratio can be confirmed by our XPS surface chemical composition analysis. In contrary, the stoichiometric excess SCN^- can not be obtained easily for CuSCN without any halogen treatment. Perera et al. reported the PL peak at 350 and 460 nm of untreated CuSCN film originated from the recombination of electrons in the conduction band with holes in the valence band and SCN^- acceptor, respectively. However, the trap PL peak intensity is very small due to low excess SCN^- density.[46] We also find the PL peak at 470 nm for CuSCN film, which is quite close to the above report, but low trap PL intensity is in accordance with no severe surface trap problem for the CuSCN film. For composite films, the PL intensity at 422 and 470 nm decrease gradually with increasing proportion of CuSCN. The decreased PL intensity at 422 nm is thought to be associated with the CuI passivation from SCN^-, while the decreased PL intensity at 470 nm attributed to that stoichiometric excess SCN^- is used to passivate CuI surface, resulting in a more accurate stoichiometric ratio of the CuSCN film. In all, the impact of mixed ratios on absorbance threshold and surface state of composite films has been confirmed by absorbance and PL spectra, respectively.

3.2. Photoresponse Properties of ZnO-CuI/CuSCN Photodiode. Current density−voltage (J−V) characteristics of ZnO-CuI/CuSCN photodiode with G/AgNWs TE are shown in Figure 4. The related photoresponse parameters under 0 V are summarized in Table 1. So the photocurrent density is short-current density (J_{sc}). We can obtain low rectification ratio, on/off ratio, and V_{oc} for ZnO-CuI/CuSCN (20:1) photodiode, which is quite close to the performance of ZnO-CuI. In particular, the dark current in negative bias voltage is far higher than Schein et al.'s ZnO-CuI diode prepared by all physical method,[47] making our diode rectifying property far worse than them. On the one hand, the crack and rough morphology of CuI film by solution-processed method, we are convinced, is responsible for high dark current, and on the other hand, the surface trap of CuI increases the recombination

Table 1. Photoresponse Parameters of Five Photodiode UV Detectors with G/AgNWs TE

devices	J_d (μA/cm^2)	J_l (μA/cm^2)	on/off ratio at 0 V	V_{oc} (V)	rectification ratio at ±1 V
ZnO-CuI	0.24	9.8	41	0.02	9.5
ZnO-CuSCN	0.01	0.25	25	0.06	92.3
ZnO-CuI/CuSCN (20:1)	0.13	4.4	34	0.03	4.3
ZnO-CuI/CuSCN (10:1)	0.017	8.7	512	0.09	10
ZnO-CuI/CuSCN (5:1)	0.013	3.9	300	0.17	103

of photogenerated carriers, limiting the V_{oc}. Besides, the performance of this ZnO-CuI planar hybrid photodiode is quite close to our recent report on ZnO NWs-CuI photodiode,[48] indicating the consistency of the solution-processed device. ZnO-CuSCN photodiode has the lowest J_{sc} and on/off ratio due to low hole mobility of the CuSCN film. The high-rectification ratio can be attributed to compact CuSCN film, which is close to Garnier et al.'s report on the ZnO NWs/CuSCN heterojunction.[49] The high V_{oc} provides the evidence of low surface trap density of CuSCN, which is higher than Hatch et al.'s report.[7] Even though J_{sc} is lower than theirs due to thinner thickness of the whole device. In particular, with increasing proportion of CuSCN in composite films, the higher rectification ratio and V_{oc} can be obtained. Besides, decreased dark current causes increased on/off ratio for ZnO-CuI/CuSCN (10:1) and ZnO-CuI/CuSCN (5:1) photodiodes. Thus, improving performance can be obtained using composite p-type film with suitable proportion, resulting from high conductivity of CuI and effectively passivated surface trap from SCN^-. All these photoresponse parameters can be well-explained based on the above morphology and surface state analysis for several p-type films. The photoresponse of photodiodes with Au TE are shown in Figure S9. The performance comparison for ZnO-CuI/CuSCN using Au TE is in accordance with G/AgNWs TE.

Figure 5 compares the photoresponse of ZnO-CuI/CuSCN (10:1) photodiode with three TEs. The device with PEDOT:PSS TE can be illuminated from two sides. Device illuminated through the conventional ITO glass direction is called to be forward illuminated (Fwd) and the device illuminated from the TE side, reverse illuminated (Rev). The parameters obtained from J−V characteristics in Figure 5 (panels a and b) are summarized in Table 2. Under the Fwd, the highest J_{sc} and V_{oc} are from the photodiode using Au TE, G/AgNWs TE takes the second place, and PEDOT:PSS TE is the lowest. In order to explain this difference, the EIS results shown in Figure 5 (panels c and d) are used to investigate the interfacial charge transfer process. The high-frequency arc in the Nyquist plots is attributed to charge-transfer resistance (R_{ct}) at the TE/p-type film interface, while the low-frequency arc is attributed to recombination resistance (R_r) at the pn junction, and R_s is the sheet resistances of the bottom and top electrodes.[15,50,51] Thus, low R_{ct} and high R_r can be separately beneficial to carriers extraction and separation. From Table 2, we can see decreased R_{ct} and R_r under light compared with dark state, indicating more carriers separation and extraction. The lowest R_{ct} with PEDOT:PSS TE is beneficial to hole extraction

DOI: 10.1021/acsami.5b05222
ACS Appl. Mater. Interfaces 2015, 7, 21235−21244

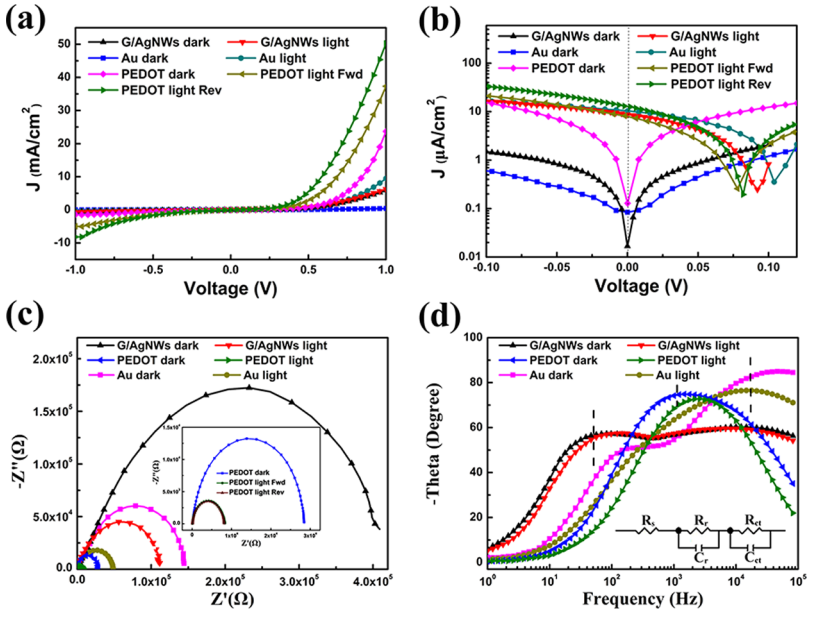

Figure 5. ZnO-CuI/CuSCN (10:1) photodiode with three kinds of TEs: (a) $J-V$ curves under dark and light conditions, (b) corresponding magnified $J-V$ curves in semilogarithmic scale near 0 V, (c) Nyquist plots, and (d) bode phase plots of corresponding devices, the peak frequencies for photodiodes using G/AgNWs, PEDOT:PSS, and Au TEs are 50, 1000, and 20000 Hz, respectively. The inset in (c) shows magnified Nyquist plots of devices with PEDOT:PSS TE. The inset in (d) is equivalent circuit for fitting EIS to obtain the value of resistance and capacitance.

Table 2. Photoresponse Parameters, Resistance, and Capacitance Values in Equivalent Circuit of Three ZnO-CuI/CuSCN (10:1) Photodiode UV Detectors with Different TEs

TEs	J_l (μA/cm^2)	on/off ratio	V_{oc} (V)	R_S (Ω)	R_r (kΩ)	C_r (nF)	R_{ct} (kΩ)	C_{ct} (nF)
Au (dark)	0.084			119	128.2	28.7	12.3	9.5
Au (light)	10.35	123	0.1	118	40.5	39.4	5.4	20.6
G/AgNWs (dark)	0.017			87	330.6	29.9	30.8	4.2
G/AgNWs (light)	8.7	512	0.09	84.4	98	36.6	7.2	19.3
PEDOT:PSS (dark)	0.1			112	27.5	46.4	0.33	83
PEDOT:PSS(Fwd)	8.2	82	0.078	88	7.8	91.6	0.23	244.1
PEDOT:PSS(Rev)	13	130	0.08	89	7.6	95.7	0.25	228.7

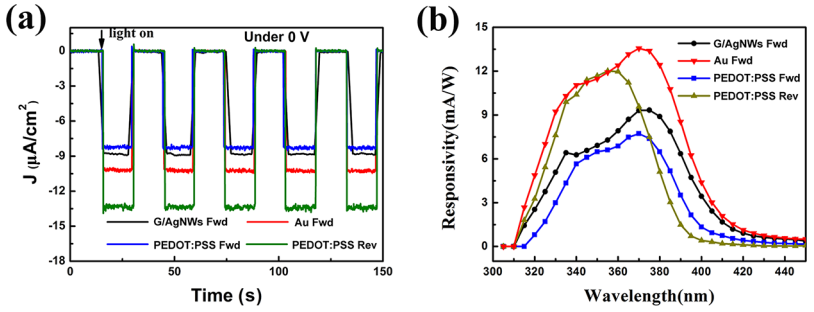

Figure 6. (a) Time-dependent photoresponse, (b) wavelength-dependent responsivity spectra of ZnO-CuI/CuSCN (10:1) photodiodes with different TEs. For device with PEDOT:PSS TE, the Fwd and Rev were conducted to compare the performance.

due to its close work function with Au,[52] but the lowest R_r can increase the recombination, decreasing both the J_{sc} and V_{oc}. High R_{ct} with G/AgNWs TE is not in favor of hole extraction, which may come from the nonclose contact using paste technique, but high R_r is beneficial to charge separation, resulting in high J_{sc} and V_{oc}. The suitable R_{ct} and R_r with Au TE are responsible for the largest J_{sc} and V_{oc}. At the same time, lower R_{ct} and R_r for Au TE compared with G/AgNWs TE under light can lead to larger photocurrent density in Figure S9. However, under the Rev, the photodiode using PEDOT:PSS TE has the highest J_{sc} compared with those devices worked under the Fwd. This can not be explained by EIS analysis, and we can find the clue from wavelength-dependent responsivity.

Furthermore, the peak frequency response in the Bode phase plots (Figure 5d) signifies the electron transfer rate at the TE/p-type film interface,[53] which can be reflected in photoresponse speed in Figure 6a. Due to the limitation of the manual switch for the on−off state, the accurate response and recovery time can not been obtained. We can observe the photodiode using G/AgNWs TE, which has the longest response time about 2 s, while response times of photodiodes using Au and PEDOT:PSS TEs are shorter than the test time interval (0.1

DOI: 10.1021/acsami.5b05222
ACS Appl. Mater. Interfaces 2015, 7, 21235−21244

Table 3. Photoresponse Parameters and Test Conditions Comparison of Different ZnO-Based UV Detectors

UV detector	structure	J_l (μA/cm^2)	on/off ratio	recovery time (s)	voltage (V)	light intensity (mW/cm^2)
ZnO/AgNWs/ZnO[5]	photoconductor	225	2787	3.67	1	mercury lamp/4.9
ZnO NWs[6]	photoconductor	1000	3000	15.44	5	xenon lamp/18
ZnO NWs-CuSCN[7]	photodiode	45	1000	6.7×10^{-6}	0	LED 380 nm/6
ZnO NWs-CuSCN[49]	photodiode	51	34	—	0	sunlight/100
ZnO -Spiro-MeOTAD[8]	photodiode	50	300	9.5×10^{-4}	0	LED 390 nm/3
ZnO-CuI/CuSCN	photodiode	13	130	< 0.1	0	xenon lamp/100

s). So response speed is in accordance with the frequency response in Figure 5d. The wavelength-dependent responsivity spectra are shown in Figure 6b. The highest responsivity for three TEs under Fwd locates at 380 nm, but the highest responsivity for PEDOT:PSS under Rev locates at 365 nm, which is closer to the band gap position of ZnO. Moreover, we measured the transmittance of several substrates in Figure S10. The results show that the transmittance of ITO glass decreases greatly with decreasing wavelength after 380 nm, and it has already decreased to 70% at 370 nm, which is equal to that of the PEDOT:PSS film on glass or quartz substrates. But the actual transmittance of the PEDOT:PSS film can be higher, which is around 77% from 300−800 nm, because the transmission loss of glass or quartz substrates are deducted. Thus, it is convinced that the low transmittance of ITO glass has greatly limited the short-wavelength UV absorption of ZnO, obtaining lower J_{sc} under Fwd than Rev. The photoresponse of ZnO-based photodiode UV detector can be further improved by increasing short-wavelength UV transmittance of a transparent electrode. On the one hand, this can be achieved by replacing common ITO glass to PEDOT:PSS on quartz or sapphire substrates in accordance with Nakano et al.'s and Xu et al.'s reports;[11,54] on the other hand, the photodiode can work under Rev by using PEDOT:PSS TE in our case because the UV transmittance loss of glass or quartz can be avoided.

Besides, the highest UV (365 nm) to visible (450 nm) rejection ratio is 179 for ZnO-CuI/CuSCN (10:1) photodiode with PEDOT:PSS TE under Rev, illustrating large responsivity at UV-A region (320−400 nm) due to high UV transmittance of PEDOT:PSS TE, and the narrow-band (60 nm) UV photoresponse resulted from the semitransparent property of photodiode with PEDOT:PSS TE. Moreover, from Table 3, our ZnO-CuI/CuSCN photodiode has faster recovery speed than comparable photoconductors and at least recovery times faster than 0.1 s, indicating the ability applying to high-speed photodetection. Finally, the stability of photodiode with three TEs is shown in Figure S11. The devices with both Au and PEDOT:PSS TEs have excellent stability in air for two months. The dark and light current of device with G/AgNWs TE decrease a little, which may be caused from an insufficient contact problem using the paste technique. The high air stability makes our ZnO-CuI/CuSCN photodiode UV detector quite promising for the future.

4. CONCLUSION

In summary, ZnO-CuI/CuSCN photodiode UV detectors with three different TEs have been fabricated. We have found that the morphology and surface state problems of CuI film could be effectively overcome by adding a suitable amount of CuSCN. On the basis of this inorganic p-type composite film, it can be observed that ZnO-CuI/CuSCN (10:1) photodiode has the largest on/off ratio of 512 and J_{sc} of 8.7 μA/cm^2, and the ZnO-CuI/CuSCN (5:1) photodiode has the largest rectification ratio of 103 at ±1 V and V_{oc} of 0.17 V using the G/AgNWs TE. Compared with photodiode using CuI or CuSCN film, the improved performance using p-type composite films can be obtained, resulting from p-type composite films combining high conductivity of CuI and low surface trap density of CuSCN, providing one strategy to improve photovoltaic performance using inorganic p-type materials. This explanation is supported by the XPS, XRD, and PL analysis of composite film. We also find that the ZnO-CuI/CuSCN (10:1) photodiode with Au TE has the largest J_{sc} and V_{oc} for Fwd, because low R_{ct} and high R_r can be the most beneficial to carriers extraction and separation. However, the photodiode with PEDOT:PSS TE under Rev has the highest J_{sc} of 13 μA/cm^2 and UV to visible rejection ratio of 179, resulting from larger responsivity at the UV region due to higher UV transmittance of PEDOT:PSS TE compared with ITO glass. Finally, the photodiode with PEDOT:PSS TE has narrow-band UV photoresponse (60 nm), reducing false alarm probability and high air stability, which is a promising candidate in the UV-A detection field.

■ ASSOCIATED CONTENT

Supporting Information

The Supporting Information is available free of charge on the ACS Publications website at DOI: 10.1021/acsami.5b05222.

SEM images of G/AgNWs TE; light source spectra; transmittance spectra of several substrates; cross-section SEM images of devices; SEM and AFM images of ZnO film layer and five p-type films; surface chemical composition of five p-type films; XRD patterns of five p-type films treated at 80 °C; J−V curves of photodiodes using Au TE; and photoresponse stability of ZnO-CuI/CuSCN (10:1) photodiode using three TEs (PDF)

■ AUTHOR INFORMATION

Corresponding Author

*E-mail: mqwang@mail.xjtu.edu.cn. Tel: +86-29-82668794.

Notes

The authors declare no competing financial interest.

■ ACKNOWLEDGMENTS

This work has been partially supported by the NSFC Major Research Plan on Nanomanufacturing (Grant 91323303). The authors gratefully acknowledge financial support from Natural Science Foundation of China (Grants 51572216 and 61176056), 111 program (no. B14040) and the open projects from Institute of Photonics and Photo-Technology, Provincial Key Laboratory of Photoelectronic Technology, Northwest University, China. The SEM work was done at ICDR, Xi'an jiaotong University, Xi'an, China. The authors also thank Ms. Dai for her help in using SEM and EDS.

DOI: 10.1021/acsami.5b05222
ACS Appl. Mater. Interfaces 2015, 7, 21235−21244

REFERENCES

(1) Tian, W.; Lu, H.; Li, L. Nanoscale ultraviolet photodetectors based on onedimensional metal oxide nanostructures. *Nano Res.* **2015**, *8*, 382−405.

(2) Monroy, E.; Omnès, F.; Calle, F. Wide-bandgap semiconductor ultraviolet photodetectors. *Semicond. Sci. Technol.* **2003**, *18*, R33−R51.

(3) Konstantatos, G.; Sargent, E. H. Nanostructured materials for photon detection. *Nat. Nanotechnol.* **2010**, *5*, 391−400.

(4) Peng, L.; Hu, L.; Fang, X. Energy Harvesting for Nanostructured Self-Powered Photodetectors. *Adv. Funct. Mater.* **2014**, *24*, 2591−2610.

(5) Yang, Z.; Wang, M.; Song, X.; Yan, G.; Ding, Y.; Bai, J. High-performance ZnO/Ag Nanowire/ZnO composite film UV photodetectors with large area and low operating voltage. *J. Mater. Chem. C* **2014**, *2*, 4312−4319.

(6) Su, Y.-K.; Peng, S.; Ji, L.; Wu, C.; Cheng, W.; Liu, C. Ultraviolet ZnO nanorod photosensors. *Langmuir* **2010**, *26*, 603−606.

(7) Hatch, S. M.; Briscoe, J.; Dunn, S. A Self-Powered ZnO-Nanorod/CuSCN UV Photodetector Exhibiting Rapid Response. *Adv. Mater.* **2013**, *25*, 867−871.

(8) Game, O.; Singh, U.; Kumari, T.; Banpurkar, A.; Ogale, S. ZnO (N)-Spiro-MeOTAD hybrid photodiode: an efficient self-powered fast-response UV (visible) photosensor. *Nanoscale* **2014**, *6*, 503−513.

(9) Lu, M.-P.; Lu, M.-Y.; Chen, L.-J. p-Type ZnO nanowires: From synthesis to nanoenergy. *Nano Energy* **2012**, *1*, 247−258.

(10) Bilgaiyan, A.; Dixit, T.; Palani, I.; Singh, V. Improved Photoresponse of Hybrid ZnO/P3HT Bilayered Photodetector Obtained Through Oriented Growth of ZnO Nanorod Arrays and the Use of Hole Injection Layer. *J. Electron. Mater.* **2015**, *44*, 2842−2848.

(11) Nakano, M.; Makino, T.; Tsukazaki, A.; Ueno, K.; Ohtomo, A.; Fukumura, T.; Yuji, H.; Akasaka, S.; Tamura, K.; Nakahara, K.; et al. Transparent polymer Schottky contact for a high performance visible-blind ultraviolet photodiode based on ZnO. *Appl. Phys. Lett.* **2008**, *93*, 123309.

(12) Shen, Y.; Yan, X.; Bai, Z.; Zheng, X.; Sun, Y.; Liu, Y.; Lin, P.; Chen, X.; Zhang, Y. A self-powered ultraviolet photodetector based on solution-processed p-NiO/n-ZnO nanorod array heterojunction. *RSC Adv.* **2015**, *5*, 5976−5981.

(13) Hsueh, H.; Chang, S.; Weng, W.; Hsu, C.; Hsueh, T.; Hung, F.; Wu, S.; Dai, B. Fabrication and characterization of coaxial p-copper oxide/n-ZnO nanowire photodiodes. *IEEE Trans. Nanotechnol.* **2012**, *11*, 127−133.

(14) Al-Hardan, N.; Jalar, A.; Hamid, M. A.; Keng, L. K.; Ahmed, N.; Shamsudin, R. A wide-band UV photodiode based on n-ZnO/p-Si heterojunctions. *Sens. Actuators, A* **2014**, *207*, 61−66.

(15) Christians, J. A.; Fung, R. C.; Kamat, P. V. An inorganic hole conductor for organo-lead halide perovskite solar cells. Improved hole conductivity with copper iodide. *J. Am. Chem. Soc.* **2014**, *136*, 758−764.

(16) Qin, P.; Tanaka, S.; Ito, S.; Tetreault, N.; Manabe, K.; Nishino, H.; Nazeeruddin, M. K.; Grätzel, M. Inorganic hole conductor-based lead halide perovskite solar cells with 12.4% conversion efficiency. *Nat. Commun.* **2014**, *5*, 3834−3839.

(17) Li, M. H.; Shen, P. S.; Wang, K. C.; Guo, T. F.; Chen, P. Inorganic P-type contact materials for perovskite-based solar cells. *J. Mater. Chem. A* **2015**, *3*, 9011−9019.

(18) Ito, S.; Tanaka, S.; Nishino, H. Lead-Halide Perovskite Solar Cells by CH3NH3I-Dripping on PbI2-CH3NH3I-DMSO Precursor Layer for Planar and Porous Structures using CuSCN Hole Transporting Material. *J. Phys. Chem. Lett.* **2015**, *6*, 881−886.

(19) Grundmann, M.; Schein, F. L.; Lorenz, M.; Böntgen, T.; Lenzner, J.; von Wenckstern, H. Cuprous iodide: A p-type transparent semiconductor: history and novel applications. *Phys. Status Solidi A* **2013**, *210*, 1671−1703.

(20) Jaffe, J. E.; Kaspar, T. C.; Droubay, T. C.; Varga, T.; Bowden, M. E.; Exarhos, G. J. Electronic and defect structures of CuSCN. *J. Phys. Chem. C* **2010**, *114*, 9111−9117.

(21) Pattanasattayavong, P.; Ndjawa, G. O. N.; Zhao, K.; Chou, K. W.; Yaacobi-Gross, N.; O'Regan, B. C.; Amassian, A.; Anthopoulos, T. D. Electric field-induced hole transport in copper (I) thiocyanate (CuSCN) thin-films processed from solution at room temperature. *Chem. Commun.* **2013**, *49*, 4154−4156.

(22) Premalal, E.; Dematage, N.; Kumara, G.; Rajapakse, R.; Shimomura, M.; Murakami, K.; Konno, A. Preparation of structurally modified, conductivity enhanced-p-CuSCN and its application in dye-sensitized solid-state solar cells. *J. Power Sources* **2012**, *203*, 288−296.

(23) Boix, P. P.; Larramona, G.; Jacob, A.; Delatouche, B.; Mora-Seró, I.; Bisquert, J. Hole transport and recombination in all-solid Sb2S3-sensitized TiO2 solar cells using CuSCN as hole transporter. *J. Phys. Chem. C* **2012**, *116*, 1579−1587.

(24) Kozhummal, R.; Yang, Y.; Güder, F.; Küçükbayrak, U. M.; Zacharias, M. Antisolvent Crystallization Approach to Construction of CuI Superstructures with Defined Geometries. *ACS Nano* **2013**, *7*, 2820−2828.

(25) Kumara, G.; Kaneko, S.; Okuya, M.; Tennakone, K. Fabrication of dye-sensitized solar cells using triethylamine hydrothiocyanate as a CuI crystal growth inhibitor. *Langmuir* **2002**, *18*, 10493−10495.

(26) Moon, I. K.; Kim, J. I.; Lee, H.; Hur, K.; Kim, W. C.; Lee, H. 2D graphene oxide nanosheets as an adhesive over-coating layer for flexible transparent conductive electrodes. *Sci. Rep.* **2013**, *3*, 1038−1045.

(27) Liang, J.; Li, L.; Tong, K.; Ren, Z.; Hu, W.; Niu, X.; Chen, Y.; Pei, Q. Silver nanowire percolation network soldered with graphene oxide at room temperature and its application for fully stretchable polymer light-emitting diodes. *ACS Nano* **2014**, *8*, 1590−1600.

(28) Chen, R.; Das, S. R.; Jeong, C.; Khan, M. R.; Janes, D. B.; Alam, M. A. Co-Percolating Graphene-Wrapped Silver Nanowire Network for High Performance, Highly Stable, Transparent Conducting Electrodes. *Adv. Funct. Mater.* **2013**, *23*, 5150−5158.

(29) Kang, J.; Jang, Y.; Kim, Y.; Cho, S.-H.; Suhr, J.; Hong, B. H.; Choi, J.-B.; Byun, D. An Ag-grid/graphene hybrid structure for large-scale, transparent, flexible heaters. *Nanoscale* **2015**, *7*, 6567−6573.

(30) Chen, J.; Bi, H.; Sun, S.; Tang, Y.; Zhao, W.; Lin, T.; Wan, D.; Huang, F.; Zhou, X.; Xie, X.; et al. Highly conductive and flexible paper of 1D silver-nanowire-doped graphene. *ACS Appl. Mater. Interfaces* **2013**, *5*, 1408−1413.

(31) Liu, Z.; Parvez, K.; Li, R.; Dong, R.; Feng, X.; Müllen, K. Transparent Conductive Electrodes from Graphene/PEDOT: PSS Hybrid Inks for Ultrathin Organic Photodetectors. *Adv. Mater.* **2015**, *27*, 669−675.

(32) Bryant, D.; Greenwood, P.; Troughton, J.; Wijdekop, M.; Carnie, M.; Davies, M.; Wojciechowski, K.; Snaith, H. J.; Watson, T.; Worsley, D. A Transparent Conductive Adhesive Laminate Electrode for High-Efficiency Organic-Inorganic Lead Halide Perovskite Solar Cells. *Adv. Mater.* **2014**, *26*, 7499−7504.

(33) Eperon, G. E.; Bryant, D.; Troughton, J.; Stranks, S. D.; Johnston, M. B.; Watson, T.; Worsley, D. A.; Snaith, H. J. Efficient, Semitransparent Neutral-Colored Solar Cells Based on Microstructured Formamidinium Lead Trihalide Perovskite. *J. Phys. Chem. Lett.* **2015**, *6*, 129−138.

(34) Leijtens, T.; Eperon, G. E.; Pathak, S.; Abate, A.; Lee, M. M.; Snaith, H. J. Overcoming ultraviolet light instability of sensitized TiO2 with meso-superstructured organometal tri-halide perovskite solar cells. *Nat. Commun.* **2013**, *4*, 2885−2892.

(35) Ghosh, T.; Basak, D. Highly efficient ultraviolet photodetection in nanocolumnar RF sputtered ZnO films: a comparison between sputtered, sol−gel and aqueous chemically grown nanostructures. *Nanotechnology* **2010**, *21*, 375202.

(36) Liu, K.; Chen, S.; Luo, Y.; Liu, L. Hybrid of silver nanowire and pristine-graphene by liquid-phase exfoliation for synergetic effects on electrical conductive composites. *RSC Adv.* **2014**, *4*, 41876−41885.

(37) Fortunato, E. M.; Barquinha, P. M.; Pimentel, A.; Gonçalves, A. M.; Marques, A. J.; Pereira, L. M.; Martins, R. F. Fully Transparent ZnO Thin-Film Transistor Produced at Room Temperature. *Adv. Mater.* **2005**, *17*, 590−594.

DOI: 10.1021/acsami.5b05222
ACS Appl. Mater. Interfaces 2015, 7, 21235−21244

(38) Carcia, P.; McLean, R.; Reilly, M.; Nunes, G., Jr Transparent ZnO thin-film transistor fabricated by rf magnetron sputtering. *Appl. Phys. Lett.* **2003**, *82*, 1117−1119.
(39) Inudo, S.; Miyake, M.; Hirato, T. Electrical properties of CuI films prepared by spin coating. *Phys. Status Solidi A* **2013**, *210*, 2395−2398.
(40) Yang, Y.; Gao, Q. Growth and photoluminescence characterization of highly oriented CuI/β-cyclodextrin hybrid composite film. *Langmuir* **2005**, *21*, 6866−6871.
(41) Zheng, Z.; Liu, A.; Wang, S.; Huang, B.; Wong, K. W.; Zhang, X.; Hark, S. K.; Lau, W. M. Growth of highly oriented (110) γ-CuI film with sharp exciton band. *J. Mater. Chem.* **2008**, *18*, 852−854.
(42) Yin, X.; Que, W.; Fei, D.; Xie, H.; He, Z.; Wang, G. Strategies to prepare an efficient photoanode for ZnO nanowires-based CdS−CdSe co-sensitized solar cells. *Electrochim. Acta* **2013**, *89*, 561−570.
(43) Song, X.; Wang, M.; Deng, J.; Yang, Z.; Ran, C.; Zhang, X.; Yao, X. One-Step Preparation and Assembly of Aqueous Colloidal CdS_xSe_{1-x} Nanocrystals within Mesoporous TiO2 Films for Quantum Dot-Sensitized Solar Cells. *ACS Appl. Mater. Interfaces* **2013**, *5*, 5139−5148.
(44) Pan, J.; Utama, M. I. B.; Zhang, Q.; Liu, X.; Peng, B.; Wong, L. M.; Sum, T. C.; Wang, S.; Xiong, Q. Composition-Tunable Vertically Aligned CdS_xSe_{1-x} Nanowire Arrays via van der Waals Epitaxy: Investigation of Optical Properties and Photocatalytic Behavior. *Adv. Mater.* **2012**, *24*, 4151−4156.
(45) Perera, V.; Tennakone, K. Recombination processes in dye-sensitized solid-state solar cells with CuI as the hole collector. *Sol. Energy Mater. Sol. Cells* **2003**, *79*, 249−255.
(46) Perera, V.; Senevirathna, M.; Pitigala, P.; Tennakone, K. Doping CuSCN films for enhancement of conductivity: Application in dye-sensitized solid-state solar cells. *Sol. Energy Mater. Sol. Cells* **2005**, *86*, 443−450.
(47) Schein, F.-L.; von Wenckstern, H.; Grundmann, M. Transparent p-CuI/n-ZnO heterojunction diodes. *Appl. Phys. Lett.* **2013**, *102*, 092109.
(48) Yang, Z.; Wang, M.; Shukla, S.; Zhu, Y.; Deng, J.; Ge, H.; Wang, X.; Xiong, Q. Developing Seedless Growth of ZnO Micro/Nanowire Arrays towards ZnO/FeS2/CuI P-I-N Photodiode Application. *Sci. Rep.* **2015**, *5*, 11377−11387.
(49) Garnier, J. D.; Parize, R.; Appert, E.; Chaix-Pluchery, O.; Kaminski-Cachopo, A.; Consonni, V. Physical Properties of Annealed ZnO Nanowire/CuSCN Heterojunctions for Self-Powered Ultra-Violet Photodetectors. *ACS Appl. Mater. Interfaces* **2015**, *7*, 5820−5829.
(50) Etgar, L.; Moehl, T.; Gabriel, S.; Hickey, S. G.; Eychmüller, A.; Grätzel, M. Light energy conversion by mesoscopic PbS quantum dots/TiO2 heterojunction solar cells. *ACS Nano* **2012**, *6*, 3092−3099.
(51) Ambade, S. B.; Ambade, R. B.; Lee, W.; Mane, R. S.; Yoon, S. C.; Lee, S.-H. Development of highly transparent seedless ZnO nanorods engineered for inverted polymer solar cells. *Nanoscale* **2014**, *6*, 12130−12141.
(52) Sun, K.; Zhang, S.; Li, P.; Xia, Y.; Zhang, X.; Du, D.; Isikgor, F. H.; Ouyang, J. Review on application of PEDOTs and PEDOT:PSS in energy conversion and storage devices. *J. Mater. Sci.: Mater. Electron.* **2015**, *26*, 4438−4462.
(53) Song, X.; Wang, M.; Deng, J.; Ju, Y.; Xing, T.; Ding, J.; Yang, Z.; Shao, J. ZnO/PbS core/shell nanorod arrays as efficient counter electrode for quantum dot-sensitized solar cells. *J. Power Sources* **2014**, *269*, 661−670.
(54) Xu, Y.; Wang, Y.; Liang, J.; Huang, Y.; Ma, Y.; Wan, X.; Chen, Y. A hybrid material of graphene and poly (3, 4-ethyldioxythiophene) with high conductivity, flexibility, and transparency. *Nano Res.* **2009**, *2*, 343−348.

DOI: 10.1021/acsami.5b05222
ACS Appl. Mater. Interfaces 2015, 7, 21235−21244